

CDXFormer: Boosting Remote Sensing Change Detection with Extended Long Short-Term Memory

Zhenkai Wu¹, Xiaowen Ma^{1,2}, Rongrong Lian¹, Zhentao Lin⁴ and Wei Zhang^{1,3*}

¹School of Software Technology, Zhejiang University, Hangzhou, China

²Huawei Noah's Ark Lab, Shanghai, China

³Innovation Center of Yangtze River Delta, Zhejiang University, Jiaxing, China

⁴Guangdong University of Technology, Guangzhou, China

Email: {wuzk, xwma, lianrr, cstzhangwei}@zju.edu.cn, linzt@mail2.gdut.edu.cn

Abstract—In complex scenes and varied conditions, effectively integrating spatial-temporal context is crucial for accurately identifying changes. However, current RS-CD methods lack a balanced consideration of performance and efficiency. CNNs lack global context, Transformers have quadratic computational complexity, and Mambas are restricted by CUDA acceleration. In this paper, we propose CDXFormer, with a core component that is a powerful XLSTM-based feature enhancement layer, integrating the advantages of linear computational complexity, global context perception, and strong interpret-ability. Specifically, we introduce a scale-specific Feature Enhancer layer, incorporating a Cross-Temporal Global Perceptron customized for semantic-accurate deep features, and a Cross-Temporal Spatial Refiner customized for detail-rich shallow features. Additionally, we propose a Cross-Scale Interactive Fusion module to progressively interact global change representations with spatial responses. Extensive experimental results demonstrate that CDXFormer achieves state-of-the-art performance across three benchmark datasets, offering a compelling balance between efficiency and accuracy. Code is available at <https://github.com/xwmaxwma/rschange>.

Index Terms—Remote Sensing Change Detection, Extended Long Short-Term Memory, Spatio-Temporal Interaction.

I. INTRODUCTION

The rapid progress in Earth observation technology, including advancements in remote sensing platforms and sensors, has expanded the ability to monitor surface activities. Remote Sensing Change Detection (RS-CD) focuses on identifying changes in objects of interest by comparing images of the same area taken at different times. This enables both quantitative and qualitative assessments of geographical and environmental changes, with applications in urban planning [1], disaster assessment [2], and environmental monitoring [3].

RS-CD tasks are inherently multi-scale and multi-temporal, with effective change detection relying on the aggregation of spatial and temporal context. Traditional methods—algebraic-based [4], [5], transformation-based [6]–[8], and classification-based [9], [10]—depend heavily on handcrafted features, which struggle with complex environments and limited information aggregation. CNN-based methods introduced deep learning to RS-CD by designing multi-scale feature fusion structures for improved spatio-temporal modeling [11], [12]. Techniques like deeper CNNs [3], [13], [14], dilated convolutions [15], attention mechanisms [16]–[18], multi-scale convolutions [19], and 3D convolution's inner fusion properties [20] have been explored, but challenges remain in modeling long-range dependencies. After that, Transformer-based methods have gained traction for RS-CD due to their global self-attention mechanism, which models dependencies across spatio-temporal feature maps [21], [22]. These approaches focus on cross-scale [23] and cross-temporal fusion [24],

achieving strong results in global spatio-temporal modeling. However, these methods often suffer from quadratic computational complexity caused by the self-attention calculation.

Recently, Mamba-based methods [25] have gained rapid popularity for their linear complexity and global perception capabilities. While they offer a competitive solution, their reliance on CUDA acceleration and suboptimal performance remain limitations. In response, XLSTM has emerged with its exponential gating mechanism and matrix-parallel memory [26], [27], combining the advantages of Mamba with parallel acceleration and enhanced interpret-ability. We aim to explore the application of XLSTM in RS-CD for the first time, enabling models to capture change representations more intuitively and efficiently.

In this paper, we evaluate the strengths and limitations of CNNs, Transformers, and Mambas, while highlighting the potential of XLSTM for RS-CD tasks. First, bi-temporal images generate multi-scale feature maps through a Siamese backbone. The core component of CDXFormer is a powerful XLSTM-based feature enhancement (FE) layer that specifically incorporates scale-specific scanning strategies. Specifically, Cross-Temporal Global Perceptron (CTGP) is introduced at the deeper layer aiming to enhance the semantic differences of the objects of interest in the bi-temporal image based on global perception. Considering that shallow features are relatively semantically inaccurate and rich in spatial details, Cross-Temporal Spatial Refiner (CTSR) is introduced at the shallow layer, which reduces the interference of background pixels and complements the spatial response to variations through axial scanning. Specifically, we employed a shared-parameter bidirectional scanning mLSTM block [27] (Bi-mLSTM). Finally, we recognize that the largest-scale branch, with its comprehensive spatial information, is crucial for accurate change detection. We propose a Cross-scale Interactive Fusion module (CSIF), which uses the largest-scale branch as a foundation to progressively integrate spatial information and global semantics from smaller-scale branches. Overall, our contributions can be summarized as follows:

- 1) We analyze the strengths and potential of XLSTM in comparison to CNNs, Transformers, and Mambas, and applied it to RS-CD tasks for the first time. With its linear complexity, global context awareness, parallel acceleration, and enhanced interpret-ability, XLSTM enables more intuitive and efficient differentiation of changes of interest.
- 2) We customize a scale-specific XLSTM scanning strategy for RS-CD tasks to reduce redundancy. Specifically, we propose a Cross-Temporal Global Perceptron (CTGP) and a Cross-Temporal Spatial Refiner (CTSR) to effectively capture both local spatial details and global contextual changes.

* Corresponding authors.

This work was supported by the Science and Technology Innovation 2025 Major Project of Ningbo City (Grant No. 2022Z032).

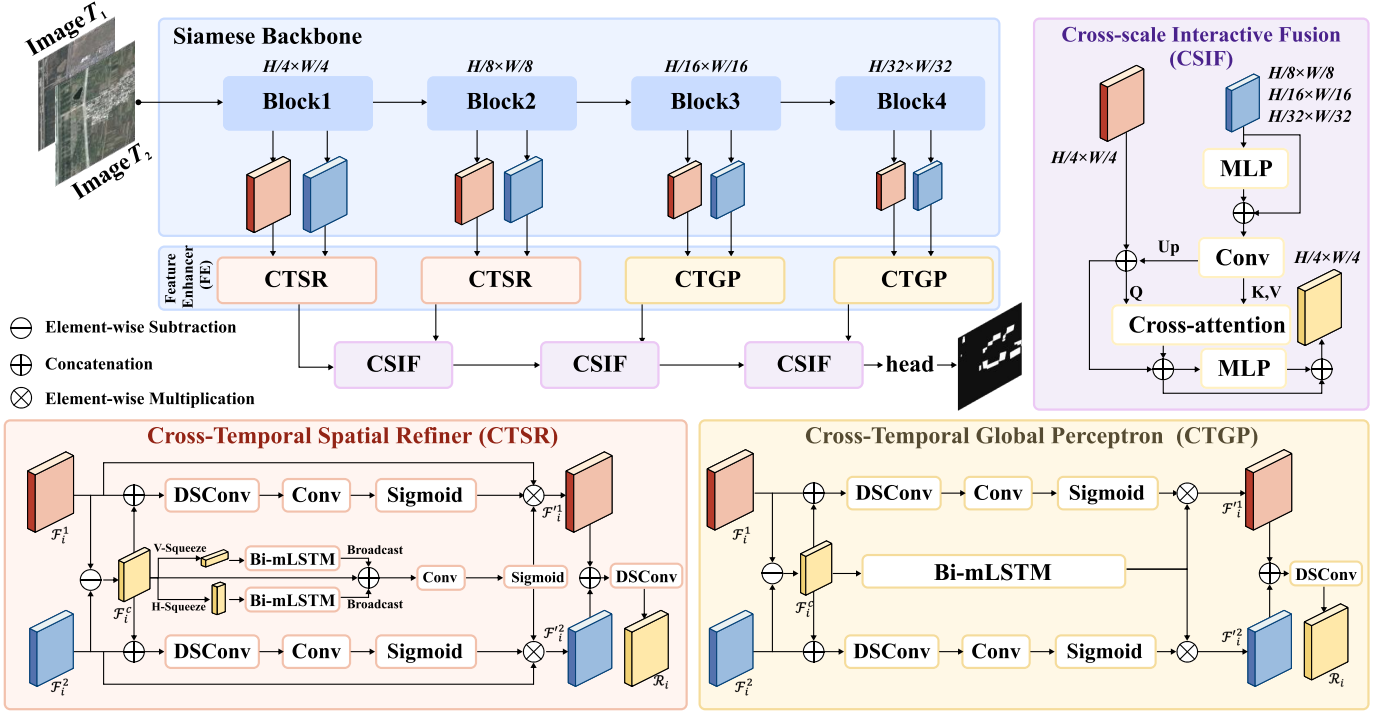


Fig. 1. Overall architecture of CDXFormer, which consists of a Siamese backbone, a Feature Enhancer (FE) layer, and a Cross-scale Interactive Fusion (CSIF) module. We introduce Cross-Temporal Spatial Refiner (CTSR) blocks and Cross-Temporal Global Perceptron (CTGP) blocks in the FE layer to extract bi-temporal features, focusing on spatial details and global context, respectively. Here, Bi-mLSTM refers to an mLSTM module that performs bidirectional scanning. Then, the CSIF module facilitates sufficient interaction between cross-scale features.

- 3) We propose a Cross-scale Interactive Fusion module (CSIF) to progressively integrate spatial information and global semantics.
- 4) Our experiments on three RS-CD benchmark datasets demonstrate that CDXFormer surpasses previous SOTA approaches, achieving a superior balance between accuracy and efficiency.

II. METHODOLOGY

Leveraging XLSTM’s linear complexity, global context awareness, parallel acceleration, and enhanced interpret-ability [26], we designed a scale-specific CDXFormer that effectively models change representations while reducing redundancy. In the following subsections, we first outline the overall architecture (Sec. II-A) of CDXFormer, followed by a detailed introduction to the Feature Enhancer (FE) (Sec. II-B) components: the Cross-Temporal Global Perceptron (CTGP) (Sec. II-B1) for the low-resolution branch and the Cross-Temporal Spatial Refiner (CTSR) (Sec. II-B2) for the high-resolution branch. We then present the Cross-scale Interactive Fusion module (CSIF) (Sec. II-C). Finally, we describe the design of the loss function (Sec. II-D).

A. Overall Architecture

We propose CDXFormer (outlined in Fig. 1), which strikes a good balance between performance and efficiency. It employs a scale-specific XLSTM scanning strategy that effectively addresses differences between scales, further enhancing overall performance.

Specifically, CDXFormer includes a Siamese backbone, a FE layer (with CTGP and CTSR), and a CSIF module. Features are extracted using weight-shared Seaformer-L [28] Siamese backbones, with the low-resolution branch capturing global semantics via CTGP and the high-resolution branch enhancing spatial details via CTSR. Finally, the CSIF module enables effective multi-scale feature interaction.

B. Feature Enhancer

This section introduces the design concept of the Feature Enhancer. We believe the low-resolution branch, with its global perspective, should primarily be used to differentiate between change regions and background in bi-temporal features. In contrast, the high-resolution branch, rich in spatial details, should focus on enhancing spatial responses, which is crucial for accurately locating change regions. Therefore, we designed the Cross-Temporal Global Perceptron (CTGP) for the low-resolution branch and the Cross-Temporal Spatial Refiner (CTSR) for the high-resolution branch, each tailored to their specific roles.

1) *Cross-Temporal Global Perceptron*: This block is designed for the low-resolution branch to capture global change semantics. Given the low-resolution bi-temporal features F_i^1 and F_i^2 extracted by the Siamese backbones, we first compute the coarse global change representation F_i^c through element-wise subtraction:

$$F_i^c = F_i^1 \ominus F_i^2 \quad (1)$$

Next, F_i^c is concatenated with each of the bi-temporal features separately. This is followed by a deep separable convolution (DSCConv) and a sigmoid activation function (σ), enabling the model to learn finer spatial details and generate more accurate weights, resulting in W_i^1 and W_i^2 , as shown in Eq. 2.

$$W_i^t = \sigma(\text{Conv}(\text{DSCConv}(F_i^c \oplus F_i^t))), t \in \{1, 2\} \quad (2)$$

At the same time, we introduce an mLSTM module to directly apply long-term modeling to F_i^c in order to enhance the global change representation. Since images are unordered, we use a bidirectional mLSTM (Bi-mLSTM, represented by Φ) with shared parameters.

TABLE I

COMPARISON OF PERFORMANCE FOR RSCD ON LEVIR-CD, WHU-CD, AND CLCD DATASETS. HIGHEST SCORES ARE IN BOLD. ALL SCORES ARE IN PERCENTAGE. FLOPS ARE COUNTED WITH IMAGE SIZE OF $256 \times 256 \times 3$.

Method	Params (M)	Flops (G)	LEVIR-CD					WHU-CD					CLCD				
			F1	Pre.	Rec.	IoU	OA	F1	Pre.	Rec.	IoU	OA	F1	Pre.	Rec.	IoU	OA
FC-EF [29]	1.10	1.55	83.4	86.91	80.17	71.53	98.39	72.01	77.69	67.10	56.26	92.07	48.64	73.34	36.29	32.14	94.30
FC-Siam-Di [29]	1.35	4.25	86.31	89.53	83.31	75.92	98.67	58.81	47.33	77.66	41.66	95.63	44.10	72.97	31.60	28.29	94.04
FC-Siam-Conc [29]	1.55	4.86	83.69	91.99	76.77	71.96	98.49	66.63	60.88	73.58	49.95	97.04	54.48	68.21	45.22	37.35	94.35
IFNet [30]	50.71	41.18	88.13	94.02	82.93	78.77	98.87	83.40	96.91	73.19	71.52	98.83	48.65	49.96	47.41	32.14	92.55
DTCDSCN [31]	41.07	14.42	87.67	88.53	86.83	78.05	98.77	71.95	63.92	82.30	56.19	97.42	60.13	62.98	57.53	42.99	94.32
BIT [22]	11.89	8.71	89.31	89.24	89.37	80.68	98.92	83.98	86.64	81.48	72.39	98.75	67.10	73.07	62.04	50.49	95.47
SNUNet [32]	12.03	46.70	88.16	89.18	87.17	78.83	98.82	83.50	85.60	81.49	71.67	98.71	66.70	73.76	60.88	50.04	95.48
ChangeStar [33]	16.77	68.52	89.30	89.88	88.72	80.66	98.90	87.01	88.78	85.31	77.00	98.70	60.75	62.23	59.34	43.63	94.3
DMATNet [34]	13.27	-	89.97	90.78	89.17	81.83	98.06	85.07	89.46	82.24	74.98	95.83	66.56	72.74	61.34	49.87	95.41
LGPNet [35]	70.99	125.79	89.37	93.07	85.95	80.78	99.00	79.75	89.68	71.81	66.33	98.33	63.03	70.54	56.96	46.01	95.03
ChangeFormer [21]	41.03	202.86	90.40	92.05	88.80	82.48	99.04	81.82	87.25	77.03	69.24	94.80	58.44	65.00	53.07	41.28	94.38
SARASNet [24]	56.89	139.9	90.44	91.42	89.48	82.55	99.11	89.55	88.68	90.44	81.08	99.05	74.70	76.68	72.83	59.62	96.33
USSFC-Net [19]	1.52	3.17	88.80	87.18	90.49	79.86	98.84	88.93	91.56	86.43	80.06	99.01	63.04	64.83	61.34	46.03	94.42
AFCF3D-Net [20]	17.64	31.58	90.44	91.18	89.72	82.55	99.03	92.07	93.56	90.62	85.30	99.28	76.92	84.20	70.79	62.49	96.84
RS-Mamba [25]	51.95	22.82	90.67	90.70	90.63	82.93	99.05	91.50	93.21	89.85	84.33	99.23	71.27	72.95	69.67	72.95	95.82
Ours	16.19	3.92	90.89	91.52	90.27	83.30	99.07	92.58	93.71	91.49	86.19	99.33	78.73	83.15	74.76	64.92	96.99

Finally, the spatial weights are used to enhance the change representations, which are then concatenated and passed through another DSConv, resulting in the final global change representation R_i . This operation is shown in Eqs. 3 and 4.

$$F_i^t = W_i^t \otimes \Phi(F_i^c), t \in \{1, 2\}; \quad (3)$$

$$R_i = DSConv(F_i^1 \oplus F_i^2) \quad (4)$$

2) *Cross-Temporal Spatial Refiner*: This block is designed for the high-resolution branch to obtain a change representation with rich spatial information. Given the high-resolution bi-temporal features F_i^1 and F_i^2 extracted by the Siamese backbones, we first obtain the coarse change representation F_i^c and spatial detail enhancement weights (W_i^1 and W_i^2) according to Eqs. 1 and 2.

Unlike CTGP, we employ axial Bi-mLSTM as an attention mechanism to model spatial details in F_i^c , particularly suited for changes of interest that predominantly occur in elongated, strip-shaped buildings. Specifically, we first apply average pooling to F_i^c along the horizontal (V_Sqz) and vertical (H_Sqz) axes, followed by a Bi-mLSTM (Φ) module for each direction. The outputs are then broadcast back to the original size and combined with F_i^c via element-wise addition. After passing through a sigmoid activation function (σ), we obtain the axial spatial enhancement weights (W_i^c), as shown in Eq. 5.

$$W_i^c = \sigma(\text{Conv}(F_i^c + \Phi(V_Sqz(F_i^c)) + \Phi(H_Sqz(F_i^c)))) \quad (5)$$

To preserve as much original spatial detail as possible, both the axial spatial weights and spatial detail enhancement weights are used to refine the original bi-temporal feature map. Finally, the enhanced bi-temporal feature maps are concatenated and processed by DSConv to produce the final change representation R_i , as shown in Eq. 6.

$$R_i = DSConv((W_i^c \otimes W_i^1 \otimes F_i^1) \oplus (W_i^c \otimes W_i^2 \otimes F_i^2)) \quad (6)$$

C. Cross-scale Interactive Fusion Module

After obtaining the scale-specific change representations, we propose a Cross-Scale Interaction Fusion (CSIF) module to combine spatial details with high-level global change semantics. To accurately

pinpoint regions of interest, the highest-resolution change representation, which retains the richest spatial details, should be used as the reference, ensuring the preservation of as much spatial detail as possible. Consequently, subsequent change representations are progressively fused with this reference using the CSIF module.

In the CSIF module, given a high-resolution change representation R_h and a low-resolution change representation R_l , we first enhance R_l using an MLP residual block to obtain R_l' . This is then upsampled and added element-wise to R_h , producing R_h' . Next, R_h' is used as the Query and R_l' as the Key and Value, with cross-attention applied to fuse the high- and low-resolution information, followed by a residual connection with R_h' . After an additional MLP residual enhancement, the aggregated representation R_h^o is obtained. This R_h^o will serve as the high-resolution change representation for the next CSIF module.

After aggregating through three CSIF modules, we obtain the final change representation R^o . This is then passed through two MLP layers, with the first layer incorporating a DSConv residual connection, resulting in the final change detection map.

D. Loss Function

CDXFormer employs a combination of binary cross-entropy loss and dice loss [36] to supervise the mask. The final loss function is a weighted sum of the mask loss and classification loss, defined as: $\mathcal{L} = \lambda_{ce}\mathcal{L}_{ce} + \lambda_{dice}\mathcal{L}_{dice}$.

III. EXPERIMENTS

A. Datasets and Implementation Details

Datasets. We perform experiments on the LEVIR-CD [37] (256×256 , 7120 images for training, 1024 images for validation, and 2048 images for test), WHU-CD [38] (256×256 , 6096 images for training, 762 images for validation, and 762 images for test), and CLCD [39] (512×512 , 360 images for training, 120 images for validation, and 120 images for test) datasets.

Implementation Details. We implement CDXFormer using PyTorch, where a workstation with a NVIDIA GTX 4090 graphics cards is employed. The initial learning rate is 0.05 and the SGD optimizer is adopted with a momentum of 0.9 and a weight decay of 0.00005.

Evaluation Metrics. We use the F1-score (F1) with regard to the change category as the main evaluation indices. The metrics contain Precision (Pre.), Recall (Rec.), Intersection over Union (IoU) of the

TABLE II
ABLATION EXPERIENCES OF THE LONG-TERM MODELING STRATEGY ON CLCD DATASET.

Strategy	F1	Pre.	Rec.	IoU	OA
CNN	76.70	82.20	71.90	62.21	96.75
Transformer	75.50	76.69	74.34	60.64	96.41
Mamba	77.76	82.46	73.58	63.62	96.87
Bi-mLSTM	78.73	83.15	74.76	64.92	96.99

TABLE III
ABLATION EXPERIENCES INVOLVING THE COMBINATION BETWEEN CTSR (\perp) AND CTGP (\odot) ON CLCD DATASET.

Feature		Enhancer		Flops (G)	F1	Pre.	Rec.	IoU	OA
1/4	1/8	1/16	1/32						
\perp	\odot	\odot	\odot	5.19	78.26	80.29	76.33	64.28	96.84
\perp	\perp	\odot	\odot	3.92	78.73	83.15	74.76	64.92	96.99
\perp	\perp	\perp	\odot	3.73	77.54	83.24	72.58	63.32	96.87
\perp	\perp	\perp	\perp	3.68	77.74	81.36	74.43	63.58	96.83

change category, and overall accuracy (OA) are also reported. These metrics are defined in the same manner as in [22].

B. Main Results

We compared our results with state-of-the-art methods across various categories, including convolution-based methods such as FC-EF [29], FC-Siam-Di [29], FC-Siam-Conc [29], IFNet [30], DTCD-SCN [31], SNUNet [32], ChangeStar (FarSeg [40]) [33], LGPNet [35], USSFC-Net [19], and AFCF3D-Net [20]; transformer-based methods including DMATNet [34], BIT [22], ChangeFormer [21], and SARASNet [24]; and the Mamba-based method RS-Mamba [25].

The proposed CDXFormer achieves superior performance across three change detection datasets, outperforming recent methods, as shown in Tables I. This comprehensive comparison underscores the performance of our approach relative to leading techniques in the field. Specifically, CDXFormer improves F1 scores by 0.22%, 1.08%, and 7.46% on the LEVIR-CD, WHU-CD, and CLCD datasets, respectively, compared to RS-Mamba. This improvement is especially notable in complex scenarios like the CLCD dataset, which features diverse object distributions and richer variations. Furthermore, CDXFormer is more efficient, with only 16.19M parameters and 3.92G Flops, significantly reducing computational cost compared to the latest methods AFCF3D-Net and RS-Mamba.

In addition, we also visualize the change maps compare with SNUNet, BIT, SARASNet, and AFCF3D-Net, as shown in Fig. 2. It can be observed that CDXFormer significantly reduces false positive and negative in complex scenarios.

C. Ablation study

Ablation of the long-term modeling strategy. We further validated the effectiveness of XLSTM in long-term modeling within the feature extraction (FE) module, as shown in Table II. We conducted experiments by replacing Bi-mLSTM with CNN (SCSEBlock in [31]), Transformer (Encoder in [41]), and Mamba (SS2D in [42]). The results showed that Bi-mLSTM delivered the best performance, further confirming XLSTM’s superior modeling capability compared to CNNs, Transformers, and Mambas.

Ablation of the combination of Feature Enhancer. To explore the optimal combination of the Feature Enhancer layer (CTSR and CTGP) for extracting change representations from high- and low-resolution branches, we conducted relevant experiments, as shown

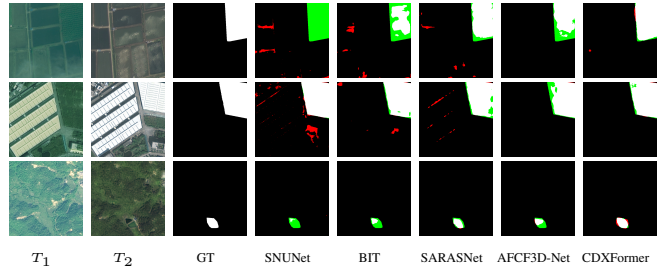


Fig. 2. Example results output on test sets from CLCD. Pixels are colored differently for better visualization (i.e., white for true positive, black for true negative, red for false positive, and green for false negative).

TABLE IV
ABLATION EXPERIENCES OF THE PROPOSED BLOCKS ON CLCD DATASET.

CTSR	CTGP	CSIF	F1	Pre.	Rec.	IoU	OA
\times	\checkmark	\checkmark	78.03	78.05	78.01	63.98	96.73
\checkmark	\times	\checkmark	76.16	83.02	70.35	61.50	96.72
\checkmark	\checkmark	\times	76.63	79.13	74.28	62.11	96.63
\checkmark	\checkmark	\checkmark	78.73	83.15	74.76	64.92	96.99

in Table III. The results indicate that the model achieves the best performance with an F1-score of 78.73% when using CTSR at 1/4 and 1/8 resolutions, and CTGP at 1/16 and 1/32 resolutions. This suggests that the customized scale-specific Feature Enhancer should reduce redundancy and noise in the first two higher-resolution branches while performing pixel-wise scanning for the latter branches to capture more global change semantics, ensuring optimal balance between performance and efficiency.

Ablation of the proposed blocks. We conducted an ablation study on each of the proposed modules CTSR, CTGP, and CSIF, as shown in Table IV. The results demonstrate that removing any of these modules leads to a decline in performance, highlighting that each module—CTSR, CTGP, and CSIF—plays a significant role in contributing to the overall effectiveness of the model.

IV. CONCLUSION

Mainstream RS-CD methods often struggle to balance performance and efficiency when relying on CNNs, transformers, and Mambas. However, CNNs are limited by their inability to effectively model global contexts, transformers are hindered by their quadratic computational complexity, and Mambas face restrictions due to their reliance on CUDA acceleration. To overcome these limitations, we propose CDXFormer, which, for the first time, introduces XLSTM, offering linear complexity, global context awareness, parallel acceleration, and enhanced interpret-ability. This novel approach aims to effectively bridge the gap between performance and efficiency in RS-CD tasks. In our exploration, we identified the importance of customizing a scale-specific Feature Enhancer with CTSR and CTGP that more effectively models change representations while reducing redundancy. Additionally, we introduced the CSIF module to preserve spatial details while integrating global semantics from low-resolution changes representations. The proposed CDXFormer achieves state-of-the-art results on three RS-CD datasets, striking a balance between accuracy and efficiency. In future work, we aim to explore lighter cross-temporal XLSTM designs to further enhance performance and efficiency.

REFERENCES

- [1] C. Marin, F. Bovolo, and L. Bruzzone, "Building change detection in multitemporal very high resolution sar images," *IEEE transactions on geoscience and remote sensing*, vol. 53, no. 5, pp. 2664–2682, 2014.
- [2] S. Mahdavi, B. Salehi, W. Huang, M. Amani, and B. Brisco, "A polar change detection index based on neighborhood information for flood mapping," *Remote Sensing*, vol. 11, no. 16, p. 1854, 2019.
- [3] P. P. De Bem, O. A. de Carvalho Junior, R. Fontes Guimarães, and R. A. Trancoso Gomes, "Change detection of deforestation in the brazilian amazon using landsat data and convolutional neural networks," *Remote Sensing*, vol. 12, no. 6, p. 901, 2020.
- [4] A. Singh, "Change detection in the tropical forest environment of northeastern india using landsat," *Remote sensing and tropical land management*, vol. 44, pp. 273–254, 1986.
- [5] W. J. Todd, "Urban and regional land use change detected by using landsat data," *J. Res. US Geol. Surv.*, vol. 5, no. 5, pp. 529–534, 1977.
- [6] T. Celik, "Unsupervised change detection in satellite images using principal component analysis and k -means clustering," *IEEE geoscience and remote sensing letters*, vol. 6, no. 4, pp. 772–776, 2009.
- [7] S. Saha, F. Bovolo, and L. Bruzzone, "Unsupervised deep change vector analysis for multiple-change detection in vhr images," *IEEE Transactions on Geoscience and Remote Sensing*, vol. 57, no. 6, pp. 3677–3693, 2019.
- [8] E. P. Crist, "A tm tasseled cap equivalent transformation for reflectance factor data," *Remote sensing of Environment*, vol. 17, no. 3, pp. 301–306, 1985.
- [9] S. Suthaharan and S. Suthaharan, "Support vector machine," *Machine learning models and algorithms for big data classification: thinking with examples for effective learning*, pp. 207–235, 2016.
- [10] D. K. Seo, Y. H. Kim, Y. D. Eo, M. H. Lee, and W. Y. Park, "Fusion of sar and multispectral images using random forest regression for change detection," *ISPRS International Journal of Geo-Information*, vol. 7, no. 10, p. 401, 2018.
- [11] X. Song, Z. Hua, and J. Li, "Remote sensing image change detection transformer network based on dual-feature mixed attention," *IEEE Transactions on Geoscience and Remote Sensing*, vol. 60, pp. 1–16, 2022.
- [12] H. Chen, Z. Qi, and Z. Shi, "Remote sensing image change detection with transformers," *IEEE Transactions on Geoscience and Remote Sensing*, vol. 60, pp. 1–14, 2021.
- [13] J. Chen, Z. Yuan, J. Peng, L. Chen, H. Huang, J. Zhu, Y. Liu, and H. Li, "Dasnet: Dual attentive fully convolutional siamese networks for change detection in high-resolution satellite images," *IEEE Journal of Selected Topics in Applied Earth Observations and Remote Sensing*, vol. 14, pp. 1194–1206, 2020.
- [14] M. Zhang and W. Shi, "A feature difference convolutional neural network-based change detection method," *IEEE Transactions on Geoscience and Remote Sensing*, vol. 58, no. 10, pp. 7232–7246, 2020.
- [15] M. Zhang, G. Xu, K. Chen, M. Yan, and X. Sun, "Triplet-based semantic relation learning for aerial remote sensing image change detection," *IEEE Geoscience and Remote Sensing Letters*, vol. 16, no. 2, pp. 266–270, 2018.
- [16] Y. Liu, C. Pang, Z. Zhan, X. Zhang, and X. Yang, "Building change detection for remote sensing images using a dual-task constrained deep siamese convolutional network model," *IEEE Geoscience and Remote Sensing Letters*, vol. 18, no. 5, pp. 811–815, 2020.
- [17] C. Zhang, P. Yue, D. Tapete, L. Jiang, B. Shangguan, L. Huang, and G. Liu, "A deeply supervised image fusion network for change detection in high resolution bi-temporal remote sensing images," *ISPRS Journal of Photogrammetry and Remote Sensing*, vol. 166, pp. 183–200, 2020.
- [18] X. Peng, R. Zhong, Z. Li, and Q. Li, "Optical remote sensing image change detection based on attention mechanism and image difference," *IEEE Transactions on Geoscience and Remote Sensing*, vol. 59, no. 9, pp. 7296–7307, 2020.
- [19] T. Lei, X. Geng, H. Ning, Z. Lv, M. Gong, Y. Jin, and A. K. Nandi, "Ultralightweight spatial-spectral feature cooperation network for change detection in remote sensing images," *IEEE Transactions on Geoscience and Remote Sensing*, vol. 61, pp. 1–14, 2023.
- [20] Y. Ye, M. Wang, L. Zhou, G. Lei, J. Fan, and Y. Qin, "Adjacent-level feature cross-fusion with 3d cnn for remote sensing image change detection," *IEEE Transactions on Geoscience and Remote Sensing*, 2023.
- [21] W. G. C. Bandara and V. M. Patel, "A transformer-based siamese network for change detection," in *IGARSS 2022-2022 IEEE International Geoscience and Remote Sensing Symposium*. IEEE, 2022, pp. 207–210.
- [22] H. Chen, Z. Qi, and Z. Shi, "Remote sensing image change detection with transformers," *IEEE Transactions on Geoscience and Remote Sensing*, vol. 60, pp. 1–14, 2021.
- [23] Y. Feng, H. Xu, J. Jiang, H. Liu, and J. Zheng, "Icif-net: Intra-scale cross-interaction and inter-scale feature fusion network for bitemporal remote sensing images change detection," *IEEE Transactions on Geoscience and Remote Sensing*, vol. 60, pp. 1–13, 2022.
- [24] C.-P. Chen, J.-W. Hsieh, P.-Y. Chen, Y.-K. Hsieh, and B.-S. Wang, "Saras-net: scale and relation aware siamese network for change detection," in *Proceedings of the AAAI Conference on Artificial Intelligence*, vol. 37, no. 12, 2023, pp. 14 187–14 195.
- [25] S. Zhao, H. Chen, X. Zhang, P. Xiao, L. Bai, and W. Ouyang, "Rsmamba for large remote sensing image dense prediction," *arXiv preprint arXiv:2404.02668*, 2024.
- [26] M. Beck, K. Pöppel, M. Spanring, A. Auer, O. Prudnikova, M. Kopp, G. Klambauer, J. Brandstetter, and S. Hochreiter, "xlstm: Extended long short-term memory," *arXiv preprint arXiv:2405.04517*, 2024.
- [27] B. Alkin, M. Beck, K. Pöppel, S. Hochreiter, and J. Brandstetter, "Vision-1stm: xlstm as generic vision backbone," *arXiv preprint arXiv:2406.04303*, 2024.
- [28] Q. Wan, Z. Huang, J. Lu, G. Yu, and L. Zhang, "Seaformer: Squeeze-enhanced axial transformer for mobile semantic segmentation," *arXiv preprint arXiv:2301.13156*, 2023.
- [29] R. C. Daudt, B. Le Saux, and A. Boulch, "Fully convolutional siamese networks for change detection," in *2018 25th IEEE International Conference on Image Processing (ICIP)*. IEEE, 2018, pp. 4063–4067.
- [30] C. Zhang, P. Yue, D. Tapete, L. Jiang, B. Shangguan, L. Huang, and G. Liu, "A deeply supervised image fusion network for change detection in high resolution bi-temporal remote sensing images," *ISPRS Journal of Photogrammetry and Remote Sensing*, vol. 166, pp. 183–200, 2020.
- [31] Y. Liu, C. Pang, Z. Zhan, X. Zhang, and X. Yang, "Building change detection for remote sensing images using a dual-task constrained deep siamese convolutional network model," *IEEE Geoscience and Remote Sensing Letters*, vol. 18, no. 5, pp. 811–815, 2020.
- [32] S. Fang, K. Li, J. Shao, and Z. Li, "Snunet-cd: A densely connected siamese network for change detection of vhr images," *IEEE Geoscience and Remote Sensing Letters*, vol. 19, pp. 1–5, 2021.
- [33] Z. Zheng, A. Ma, L. Zhang, and Y. Zhong, "Change is everywhere: Single-temporal supervised object change detection in remote sensing imagery," in *Proceedings of the IEEE/CVF international conference on computer vision*, 2021, pp. 15 193–15 202.
- [34] X. Song, Z. Hua, and J. Li, "Remote sensing image change detection transformer network based on dual-feature mixed attention," *IEEE Transactions on Geoscience and Remote Sensing*, vol. 60, pp. 1–16, 2022.
- [35] T. Liu, M. Gong, D. Lu, Q. Zhang, H. Zheng, F. Jiang, and M. Zhang, "Building change detection for vhr remote sensing images via local-global pyramid network and cross-task transfer learning strategy," *IEEE Transactions on Geoscience and Remote Sensing*, vol. 60, pp. 1–17, 2022.
- [36] F. Milletari, N. Navab, and S.-A. Ahmadi, "V-net: Fully convolutional neural networks for volumetric medical image segmentation," in *2016 fourth international conference on 3D vision (3DV)*. Ieee, 2016, pp. 565–571.
- [37] H. Chen and Z. Shi, "A spatial-temporal attention-based method and a new dataset for remote sensing image change detection," *Remote Sensing*, vol. 12, no. 10, p. 1662, 2020.
- [38] S. Ji, S. Wei, and M. Lu, "Fully convolutional networks for multisource building extraction from an open aerial and satellite imagery data set," *IEEE Transactions on Geoscience and Remote Sensing*, vol. 57, no. 1, pp. 574–586, 2018.
- [39] M. Liu, Z. Chai, H. Deng, and R. Liu, "A cnn-transformer network with multi-scale context aggregation for fine-grained cropland change detection," *IEEE Journal of Selected Topics in Applied Earth Observations and Remote Sensing*, 2022.
- [40] Z. Zheng, Y. Zhong, J. Wang, and A. Ma, "Foreground-aware relation network for geospatial object segmentation in high spatial resolution remote sensing imagery," in *Proceedings of the IEEE/CVF conference on computer vision and pattern recognition*, 2020, pp. 4096–4105.
- [41] A. Vaswani, "Attention is all you need," *Advances in Neural Information Processing Systems*, 2017.
- [42] Y. Liu, Y. Tian, Y. Zhao, H. Yu, L. Xie, Y. Wang, Q. Ye, and Y. Liu, "Vmamba: Visual state space model," *arXiv preprint arXiv:2401.10166*, 2024.